

Zeeman-splitting-induced Topological Nodal Structure and Anomalous Hall Conductivity in ZrTe_5

Yichul Choi,^{1,*} John W. Villanova,^{2,†} and Kyungwha Park^{1,‡}

¹*Department of Physics, Virginia Tech, Blacksburg, Virginia 24061, USA*

²*Department of Physics, University of Arkansas, Fayetteville, Arkansas 72701, USA*

(Dated: October 11, 2019)

We investigate the topological nodal structure of three-dimensional (3D) ZrTe_5 driven by Zeeman splitting as a function of the direction of external magnetic (\mathbf{B}) field by using a Wannier-function-based tight-binding (WFTB) model obtained from first-principles calculations. It is known that small external stimuli can drive 3D ZrTe_5 into different topological phases including Dirac semimetal. In order to emphasize the effect of Zeeman splitting, we consider 3D ZrTe_5 in a strong TI phase with a small band gap. With Zeeman splitting greater than the band gap, the WFTB model suggests that a type-I nodal ring protected by (glide) mirror symmetry is formed when the \mathbf{B} field aligns with the crystal a or b axes, and that a pair of type-I Weyl nodes are formed otherwise, when conduction and valence bands touch. We show that a pair of Weyl nodes can disappear through formation of a nodal ring, rather than requiring two Weyl nodes with opposite chirality to come together. Interestingly, a type-II nodal ring appears from crossings of the top two valence bands when the \mathbf{B} field is applied along the c axis. This nodal ring gaps out to form type-II Weyl nodes when the \mathbf{B} field rotates in the bc plane. Comparing the WFTB and linearized $k \cdot p$ model, we find inadequacy of the latter at some \mathbf{B} field directions. Further, using the WFTB model, we numerically compute the intrinsic anomalous Hall conductivity σ_{ac} induced by Berry curvature as a function of chemical potential and \mathbf{B} field direction. We find that σ_{ac} increases abruptly when the \mathbf{B} field is tilted from the a axis within the ab plane. Our WFTB model also shows significant anomalous Hall conductivity induced by avoided level crossings even in the absence of Weyl nodes.

I. INTRODUCTION

Among various three-dimensional (3D) topological materials, ZrTe_5 is unique in that small volume changes^{1,2}, small strains^{3,4}, or even moderate temperature⁵ can induce a topological phase transition from weak to strong topological insulator (TI) phase. This unique aspect may be attributed to the fact that a single ZrTe_5 layer is a two-dimensional (2D) TI¹. Before the experimental discovery of weak TI, β -type bismuth iodide (Bi_4I_4)⁶, ZrTe_5 was a first realistic candidate for a weak TI. In order to drive the material from a weak to strong TI by external means, the band gap must be closed at a critical value, which manifests Dirac semimetal⁷. However, this Dirac semimetal phase is not protected by crystal rotational symmetry like Na_3Bi and Cd_3As_2 ^{7–9} or by nonsymmorphic group symmetry like β -cristobalite BiO_2 ¹⁰. The sensitivity of the topological phase to small changes of the lattice constant or temperature, places this material as an ideal playground for exploring effects of external stimuli on topological properties. Furthermore, such sensitivity resulted in experimental observations of weak TI^{4,11,12}, strong TI^{4,13}, and Dirac semimetal phases^{14–16} in 3D ZrTe_5 .

Recent magnetotransport experiments on 3D ZrTe_5 showed interesting features including a large anomalous Hall effect as a function of the orientation of external magnetic (\mathbf{B}) field (despite the absence of magnetic order)^{17,18} as well as 3D quantum Hall effect and metal-insulator transition¹⁹. In general the intrinsic anomalous Hall effect requires contributions of nonzero Berry curvature from occupied bands^{20,21}. When the \mathbf{B} field is

rotated out of plane, the anomalous Hall resistivity was observed to abruptly increase in an antisymmetric fashion or reveal strong asymmetry as a function of the field orientation¹⁷. On the other hand, for the in-plane \mathbf{B} field, the anomalous Hall resistivity was observed to show clear antisymmetry as a function of the field orientation¹⁷. The latter feature cannot be explained by the planar Hall effect^{22,23} alone. Theoretical efforts have been so far mostly limited to understanding topological nodal structures using lowest-order effective models when the \mathbf{B} field is parallel to the crystal axes¹⁵. Very recently, Burkov²⁴ proposed an effect of mirror anomaly on the intrinsic anomalous Hall conductivity (AHC) for Dirac semimetals when the \mathbf{B} field rotates. The anomalous Hall effect observed in Ref.¹⁷ has not been theoretically understood yet.

In order to provide insight into the origin of the intriguing anomalous Hall effect, we construct a Wannier-function-based tight-binding (WFTB) model for 3D ZrTe_5 from first-principles calculations and investigate topological phase transitions induced by Zeeman splitting while ignoring Landau levels. The magnitude of the \mathbf{B} field is fixed such that the Zeeman splitting is greater than a small band gap, while the \mathbf{B} field direction is varied within the crystal ab , bc , and ac planes. The WFTB model predicts that a pair of type-I Weyl nodes are formed for any direction of \mathbf{B} field except for when the \mathbf{B} field is parallel to the a or b axes, considering crossings of the conduction and valence bands. This pair of Weyl nodes abruptly transforms into a nodal ring when the \mathbf{B} field aligns with the a or b axis, which conceptually differs from annihilation of Weyl nodes with opposite chirality

at the same k point. Interestingly, when the top two valence bands cross, the WFTB model suggests type-II topological nodal structures depending on the direction of \mathbf{B} field. We also show that the linearized $k \cdot p$ model is not enough to capture even qualitatively correct nodal structures for some \mathbf{B} field directions. We numerically compute the intrinsic AHC as a function of the orientation of \mathbf{B} field and chemical potential, using the WFTB model. Our results can be compared with the experimental antisymmetric component of the intrinsic out-of-plane AHC as a function of the tilting angle.

We present the crystal structure and symmetries of ZrTe_5 in Sec. II and construction of the WFTB model in Sec. III. We show the calculated band structures using the WFTB model in the presence of \mathbf{B} field and discuss the induced topological phases as a function of \mathbf{B} -field direction in Sec. IV. We compare our findings from the WFTB model with those from the linearized $k \cdot p$ model in Sec. V. Then we present and analyze the calculated AHC as a function of \mathbf{B} -field direction and chemical potential in Sec. VI. We summarize our conclusions in Sec. VII.

II. CRYSTAL STRUCTURE AND SYMMETRIES

A. Crystal structure

Bulk ZrTe_5 crystallizes in the orthorhombic structure with space group $Cmcm$ (No. 63), D_{2h} , where the experimental lattice constants are $a = 3.9797$, $b = 14.470$, and $c = 13.676$ Å²⁵. A primitive unit cell [Fig. 1(a) and (b)] contains two Zr and ten Te atoms. The Zr atoms (green) are located at Wyckoff position 4c, and the two Te atoms (purple) and eight Te atoms (orange) are at 4c and 8f, respectively. Each 2D zigzag layer connected along the a and c axes is well separated by $\frac{b}{2}$ and stacked along the b axis with weak van der Waals interaction. Each Zr atom is bonded with eight Te atoms [Fig. 1(b)]. We consider the following Bravais lattice vectors for the primitive unit cell: $\mathbf{a}_1 = (\frac{a}{2}, -\frac{b}{2}, 0)$, $\mathbf{a}_2 = (\frac{a}{2}, \frac{b}{2}, 0)$, $\mathbf{a}_3 = (0, 0, c)$ in Cartesian coordinates. In our convention, the a , b , and c axes are the x , y , and z axes in Cartesian coordinates. The corresponding reciprocal lattice vectors are: $\mathbf{b}_1 = 2\pi(\frac{1}{a}, -\frac{1}{b}, 0)$, $\mathbf{b}_2 = 2\pi(\frac{1}{a}, \frac{1}{b}, 0)$, and $\mathbf{b}_3 = 2\pi(0, 0, \frac{1}{c})$. The first Brillouin zone (BZ) is shown in Fig. 1(c), where $S = (0, \frac{1}{2}, 0)$, $\Gamma = (0, 0, 0)$, $Z = (0, 0, \frac{1}{2})$, $R = (0, \frac{1}{2}, \frac{1}{2})$, $Y = (-\frac{1}{2}, \frac{1}{2}, 0)$, and $T = (-\frac{1}{2}, \frac{1}{2}, \frac{1}{2})$, in fractional coordinates. These high-symmetry k points are equivalent to X , Γ , Y , M , Z , and R in Ref.¹, respectively. The zone boundary point X is located at $(\eta, \eta, 0)$, where $\eta = \frac{1}{4}(1 + \frac{a^2}{b^2})$.

In order to examine the effect of Zeeman splitting, we apply 0.25% compressive uniaxial stress along the b axis to the DFT-relaxed unstrained geometry while keeping the volume fixed, such that ZrTe_5 remains in a strong TI phase with a small band gap in the presence

of spin-orbit-coupling (SOC). For reference, the relaxed unstrained lattice constants are $a = 4.0341$, $b = 14.6998$, and $c = 13.8843$ Å. In the strained case, the lattice constants are $a = 4.0391$, $b = 14.6630$, and $c = 13.9017$ Å. The results obtained from the WFTB model correspond to the 0.25% strained structure.

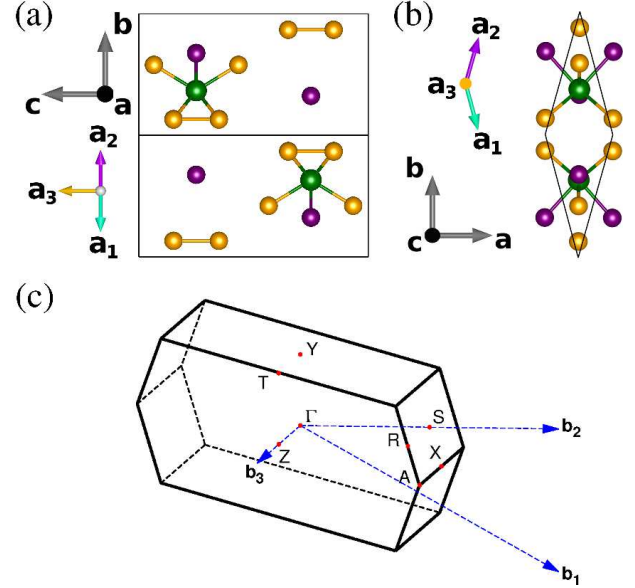


FIG. 1. (a)-(b) Side views of ZrTe_5 unit cell. Zr atoms at Wyckoff position 4c are green, and Te atoms at 4c (8f) are purple (orange). Here \mathbf{a}_1 , \mathbf{a}_2 , and \mathbf{a}_3 are the primitive cell Bravais lattice vectors. (c) First BZ with high-symmetry k points and reciprocal lattice vectors shown.

B. Symmetries

3D ZrTe_5 has inversion symmetry as well as the following crystal symmetries: two-fold rotational symmetries along the a and b axes (C_{2a} and C_{2b}), two-fold screw symmetry along the c axis, mirror symmetries about the ab and bc planes (M_{ab} , M_{bc}), and glide mirror symmetry about the ac plane (M_{ac}). Since the inversion center does not coincide with the origin of the rotational symmetries, the space group is nonsymmorphic. Inversion symmetry persists even in the presence of \mathbf{B} field. Depending on the direction of \mathbf{B} field, the following symmetries can survive: (screw) C_2 symmetry about the \mathbf{B} field direction and the (glide) mirror symmetry about the plane perpendicular to the \mathbf{B} field, or $C_{2\perp}\mathcal{T}$ where $C_{2\perp}$ is C_2 symmetry about the direction perpendicular to the \mathbf{B} field, and \mathcal{T} is the time-reversal operator.

III. CONSTRUCTION OF WANNIER-FUNCTION TIGHT-BINDING MODEL

We first calculate the electronic structure of bulk strained ZrTe_5 without SOC and \mathbf{B} field by using the density-functional theory (DFT) code VASP^{26,27}. With the DFT-calculated band structure and initial atomic orbitals, we generate Wannier functions (WFs) by using WANNIER90²⁸. Then we construct a SOC-free tight-binding model from the WFs and add atomic-like SOC to the tight-binding model such that the model-calculated band structure agrees with the DFT result. Last, we add Zeeman energy to the tight-binding model.

A. Initial DFT calculations

We perform the DFT calculations using VASP^{26,27} within the Perdew-Burke-Ernzerhof (PBE) generalized-gradient approximation (GGA)²⁹ for the exchange-correlation functional with and without SOC. We use projector augmented wave (PAW) pseudopotentials³⁰ with an energy cutoff of 350 eV and a $19 \times 19 \times 5$ Monkhorst-Pack k -point mesh. For the experimental geometry²⁵, our DFT calculation shows that bulk ZrTe_5 with SOC is in a strong TI phase with a direct band gap of about 100 meV. The structure with 0.25% compressive strain along the b axis has a band gap of 2.2 meV. All calculated band structures from the WFTB model correspond to the strained structure, unless specified otherwise.

B. SOC-free Hamiltonian

In order to construct the SOC-free WFTB model, we start with an initial set of 40 projected atomic orbitals comprised of d_{z^2} , $d_{x^2-y^2}$, d_{xy} , d_{yz} , and d_{xz} orbitals centered at two Zr sites and p_x , p_y , and p_z orbitals centered at ten Te sites in the primitive unit cell. We need to include both Zr d orbitals and Te p orbitals in the WFTB model due to their large contributions to valence and conduction bands, respectively, near Γ indicated by our DFT calculations. With the VASP-calculated Bloch eigenvalues and eigenstates, we compute the overlap matrix and projection matrix at each DFT-sampled k point by using WANNIER90^{28,31,32}. We apply the disentanglement procedure within the outer energy window $[-8.23, 5.27]$ eV relative to the Fermi level. In this energy window, the number of Bloch bands ranges from 43 to 47, and both occupied and unoccupied bands are included. We check that the generated WFs are close to pure atomic orbitals with only real components. In order to maintain the features of the atomic orbitals, maximal localization is not applied in the wannierization.

Now we construct the SOC-free WFTB model by using the generated WFs, $|\mathbf{R} + \mathbf{s}_\beta\rangle$, centered at $\mathbf{R} + \mathbf{s}_\beta$, where

\mathbf{R} are Bravais lattice vectors and \mathbf{s}_β denote the sites of orbital β ($\beta=1, \dots, 40$). The SOC-free Hamiltonian matrix \mathcal{H}_0 ³¹ reads

$$\mathcal{H}_{0,\alpha\beta}(\mathbf{k}) = \langle \psi_{\mathbf{k},\alpha} | \mathcal{H}_0 | \psi_{\mathbf{k},\beta} \rangle, \quad (1)$$

$$= \sum_{\mathbf{R}} e^{-i\mathbf{k} \cdot (\mathbf{R} + \mathbf{s}_\alpha - \mathbf{s}_\beta)} t_{\alpha\beta}(\mathbf{R} - \mathbf{0}), \quad (2)$$

$$t_{\alpha\beta}(\mathbf{R} - \mathbf{0}) = \langle \mathbf{R} + \mathbf{s}_\alpha | \mathcal{H}_0 | \mathbf{0} + \mathbf{s}_\beta \rangle, \quad (3)$$

where $|\psi_{\mathbf{k}}(\mathbf{r})\rangle$ are Bloch states over the crystal momentum \mathbf{k} space. Here $t_{\alpha\beta}(\mathbf{R} - \mathbf{0})$ is a hopping or tunneling parameter from orbital β at site \mathbf{s}_β in the home cell at $\mathbf{R} = \mathbf{0}$ to orbital α at site \mathbf{s}_α in the unit cell located at \mathbf{R} .

C. Addition of SOC and Zeeman energy

We add on-site SOC to the home-cell terms since the generated WFs are close to the atomic orbitals that we project onto. Considering the spin degrees of freedom, the number of WFs (basis set functions) is now 80. The SOC Hamiltonian becomes $\mathcal{H}_{\text{SOC}} = \lambda \mathbf{L} \cdot \boldsymbol{\sigma}$, where λ is the SOC parameter, \mathbf{L} is the orbital angular momentum, and $\boldsymbol{\sigma}$ represent Pauli spin matrices. We find that with $\lambda_{\text{Zr}} = -0.12$ eV and $\lambda_{\text{Te}} = 0.60$ eV, the WFTB calculated band structure agrees well with the VASP-calculated band structure, especially near the Γ point in the vicinity of the Fermi level.

We add the \mathbf{B} field as a Zeeman term only and do not include the Peierls phase in the hopping parameters $t_{\alpha\beta}$ because Landau levels are ignored in our calculations. Then the Zeeman interaction reads $\mathcal{H}_Z = g\mu_B \mathbf{S} \cdot \mathbf{B}$, where g is the effective electronic g factor, μ_B is Bohr magneton and \mathbf{S} is the spin angular momentum. The WFTB model has the following Hamiltonian:

$$\mathcal{H} = \mathcal{H}_0 + \mathcal{H}_{\text{SOC}} + \mathcal{H}_Z. \quad (4)$$

Hereafter we consider the Zeeman interaction energy of 10 meV unless specified otherwise. Experimental data on ZrTe_5 indicates that the g factor is highly anisotropic. The g factor when \mathbf{B} field is along the b axis (g_y) is 21.3^{15,33}, whereas the g factor for the a axis (g_x) is about 3.19³³. The g factor for the c axis (g_z) was not reported. Therefore, for \mathbf{B} field along the b axis, the Zeeman energy of 10 meV corresponds to a \mathbf{B} field of about 16 T, considering that the Zeeman energy can be expressed as $\sqrt{g_x^2 B_x^2 + g_y^2 B_y^2 + g_z^2 B_z^2} \frac{\mu_B}{2}$. As long as the Zeeman energy is greater than the band gap, the topological phase transitions presented in this work can be realized. For the strained case, the band gap of 2.2 meV implies a requisite minimum \mathbf{B} field of 3.6 T when the \mathbf{B} field is applied along the b axis.

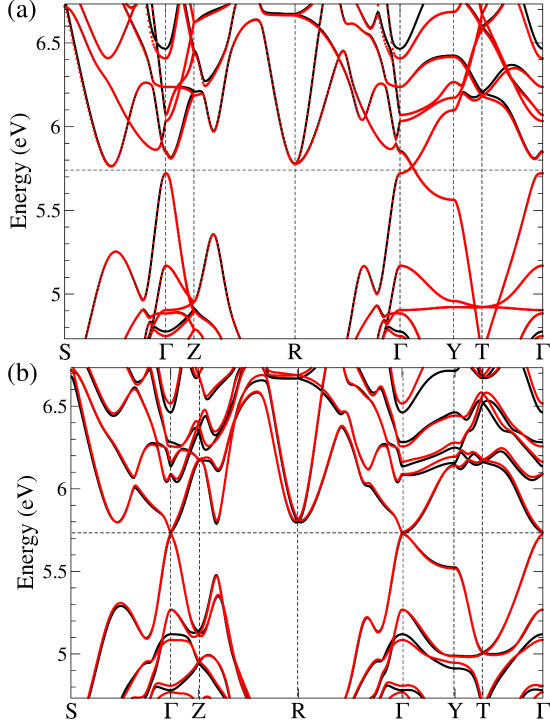


FIG. 2. (a) Comparison between the VASP-calculated (black) and the WFTB-calculated (red) band structures for strained ZrTe₅ without SOC in the primitive unit cell. (b) Likewise with SOC included. The dashed lines indicate the Fermi levels. No \mathbf{B} field is included here.

D. Comparison of WFTB-calculated to DFT-calculated band structure with and without SOC

In the absence of the Zeeman term, we compare the DFT-calculated band structure of bulk strained ZrTe₅ to the WFTB-calculated result with and without SOC, as shown in Fig. 2. Without SOC, the valence and conduction bands meet linearly at a Dirac point along the $\overline{\Gamma Y}$ direction or $\pm y$ axis. The WFTB-calculated band structure agrees well with the DFT result up to about ± 1.0 eV from the Fermi level. With SOC, a small band gap of 2.2 meV opens up at Γ which is also reliably captured by the WFTB model. We calculate the 3D topological indices $(\nu_0; \nu_1, \nu_2, \nu_3)$ ³⁴ of strained ZrTe₅ using the DFT-calculated wave function. For the reciprocal vector $\mathbf{G} = \nu_1 \mathbf{b}_1 + \nu_2 \mathbf{b}_2 + \nu_3 \mathbf{b}_3$, we find that $(\nu_0; \nu_1, \nu_2, \nu_3) = (1; 110)$. Since $\nu_0 = 1$, strained ZrTe₅ is a strong TI. Each band is at least doubly degenerate due to the inversion and time-reversal symmetries. In the $k_z = \frac{\pi}{2}$ plane, the four time-reversal invariant k points are fourfold degenerate due to the additional mirror symmetry M_{ab} .

IV. ZEEMAN-SPLITTING INDUCED TOPOLOGICAL PHASES FROM WFTB MODEL

In the presence of \mathbf{B} field, we diagonalize the 80×80 Hamiltonian matrix, Eq. (4), with the same k points as the DFT calculation. We examine the topological properties and evolution of the nodal structure as a function of \mathbf{B} -field direction for a fixed Zeeman energy of 10 meV with an isotropic g factor ($g = 2.0$) for simplicity. We consider cases that the \mathbf{B} field is applied along the a , b , and c axes as well as in the ab , bc , and ac planes. The energy window of interest is $[-0.12, +0.05]$ eV relative to the Fermi level E_F , considering that the bulk ZrTe₅ samples studied in Ref.¹⁷ are slightly hole-doped. Within this energy window, the following three types of gapless crossings are in principle possible: crossings between the bottom two conduction bands, crossings between the bottom conduction and top valence bands, and crossings between the top two valence bands. However, we do not find crossings between the bottom two conduction bands for any \mathbf{B} -field directions. We focus on the latter two types of crossing only.

A. Magnetic field along the a axis: Nodal-ring semimetal

Figure 3(a) shows the WFTB-calculated band structure along the $Y - \Gamma - Z$ direction near Γ in the vicinity of the Fermi level, when the \mathbf{B} field is applied along the a axis. The gapless points are found from crossings between the top valence and bottom conduction bands in the k_b - k_c plane and they form a ring, as shown in Fig. 3(b). Since the two bands meet with opposite slope, this is a type-I nodal ring. Note that with the \mathbf{B} field, the relevant remaining symmetries are inversion symmetry, C_{2a} and M_{bc} . From the eigenvectors of the WFTB model, we confirm that the two crossing bands have opposite M_{bc} mirror eigenvalues. The intercepts with the b and c axes are $(0, \pm 0.003072, 0)$ and $(0, 0, \pm 0.000673) 2\pi \cdot \text{\AA}^{-1}$, respectively. The gapless ring is not an equi-energy curve, and no other gapless points are found within the energy window of interest.

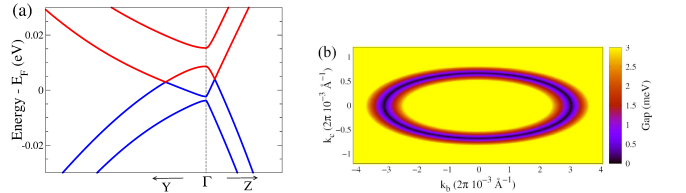


FIG. 3. (a) WFTB-calculated band structure relative to the Fermi level E_F along the $Y - \Gamma - Z$ direction when the \mathbf{B} field aligns with the a axis. (b) The corresponding gapless nodal ring in the k_b - k_c plane with the energy gap in color scale.

In order to identify the topological nature of the gapless ring, we compute the Berry phase φ_B around a closed

circle \mathcal{C} interlocking the gapless ring. The Berry phase is defined as a sum of line integrals of the Berry connection of all occupied bands n , $\mathbf{A}_n(\mathbf{k})$, over a closed path \mathcal{C} in k space:

$$\varphi_B = \sum_{n=1}^{\text{occ}} \oint_{\mathcal{C}} d\mathbf{k} \cdot \mathbf{A}_n(\mathbf{k}) \quad (5)$$

where $\mathbf{A}_n(\mathbf{k}) = i\langle u_{n\mathbf{k}} | \nabla_{\mathbf{k}} u_{n\mathbf{k}} \rangle$. Here $u_{n\mathbf{k}}$ is a periodic function of the Bloch state. We find that the Berry phase is π . Thus, the ring of the gapless points is indeed a topological nodal ring.

B. Magnetic field along the b axis: Nodal-ring semimetal

Figure 4(a) shows the calculated band structure along the $S-\Gamma-Z$ direction when the \mathbf{B} field aligns with the b axis. The bottom conduction and top valence bands meet near the Fermi level along the $\Gamma-Z$ and $\Gamma-X$ directions (not shown), whereas a small gap opens up along the $\Gamma-S$ direction. Similar to Sec. IV A, a type-I ring of gapless points is found in the k_a-k_c plane near Γ in the vicinity of the Fermi level [Fig. 4(b)]. The gapless points intercept the k_a and k_c axes at $(\pm 0.000743, 0, 0)$ and $(0, 0, \pm 0.000840) 2\pi \cdot \text{\AA}^{-1}$. We expect that the gapless crossings are allowed because the two crossing bands have opposite M_{ac} glide mirror eigenvalues. We find that the Berry phase is π ; the gapless ring is a topological nodal

ring. No other gapless crossings are found in the energy window of interest.

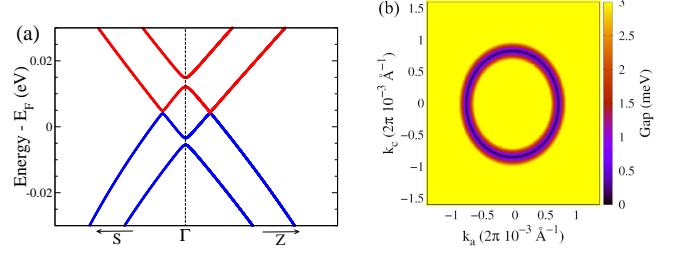


FIG. 4. (a) WFTB-calculated band structure along the $S-\Gamma-Z$ directions when \mathbf{B} field is parallel to the b axis. (b) The corresponding gapless nodal ring in the k_a-k_c plane.

C. Magnetic field along the c axis: Weyl or type-II nodal-ring semimetal

When the \mathbf{B} field aligns with the c axis, the valence and conduction bands meet with opposite slope along the c -axis at $(0, 0, \pm 0.000624) 2\pi \cdot \text{\AA}^{-1}$ in the vicinity of the Fermi level as shown in Fig. 5(a). We evaluate the topological charge χ_n associated with the gapless points by computing the Berry curvature $\Omega_n(\mathbf{k})$ using the method discussed in WANNIERTOOLS³⁵ and Ref.³⁶. The Berry curvature can be calculated as³⁷

$$\epsilon_{\alpha\beta\gamma} \Omega_{n,\gamma}(\mathbf{k}) = -2\text{Im} \sum_{m \neq n} \frac{\langle \phi_n(\mathbf{k}) | \mathcal{H}_\alpha | \phi_m(\mathbf{k}) \rangle \langle \phi_m(\mathbf{k}) | \mathcal{H}_\beta | \phi_n(\mathbf{k}) \rangle}{(\mathcal{E}_m(\mathbf{k}) - \mathcal{E}_n(\mathbf{k}))^2}, \quad (6)$$

where $\mathcal{H}_\alpha \equiv \partial \mathcal{H} / \partial k_\alpha$. Here $|\phi_n(\mathbf{k})\rangle$ and $\mathcal{E}_n(\mathbf{k})$ are the n -th eigenvector and eigenvalue of $\mathcal{H}(\mathbf{k})$ [Eq. (4)], and $\epsilon_{\alpha\beta\gamma}$ is the Levi-Civita tensor without a sum over γ . The topological charge χ_n of each gapless point (arising from a crossing of band n and band $n+1$) is then calculated by enclosing it in a small sphere \mathcal{S} ,

$$\chi_n = \frac{1}{2\pi} \oint_{\mathcal{S}} \sum_{l=1}^n d\mathbf{S} \cdot \hat{\mathbf{n}} \cdot \Omega_l(\mathbf{k}), \quad (7)$$

where $\hat{\mathbf{n}}$ is a unit vector normal to \mathcal{S} . We find that the topological charge associated with the gapless points are $\chi_n = \mp 1$, respectively, and so they are type-I Weyl points. The two Weyl points are related by inversion symmetry.

In addition, we find that the top two valence bands touch in the vicinity of the Fermi level, as shown in Fig. 5(b) and (c). The gapless points form a nodal ring in the k_a-k_b plane [Fig. 5(d)]. There are two interesting features of this ring. First, the band dispersion near

the gapless point has the same slope along the k_a and k_b axes, and so it is referred to as a type-II nodal ring. Note that the nodal ring discussed earlier in Secs. IV A and IV B is of type-I. Second, the type-II nodal ring extends to the neighboring BZ, forming a closed thin cigar shape. The size of the type-II nodal ring is much larger than the type-I nodal rings discussed in Secs. IV A and IV B. We evaluate the Berry phase around the circle interlocking the ring, finding that it is indeed π ; the ring is topologically protected by M_{ab} symmetry.

D. Magnetic field in the ab plane

Figure 6(a)-(g) schematically shows the evolution of the type-I nodal ring and Weyl points as the \mathbf{B} field rotates in the ab plane. When the \mathbf{B} field is slightly rotated from the b axis in the ab plane, the WFTB model shows that the type-I nodal ring in the k_a-k_c plane is abruptly gapped out (due to broken mirror symmetry) everywhere

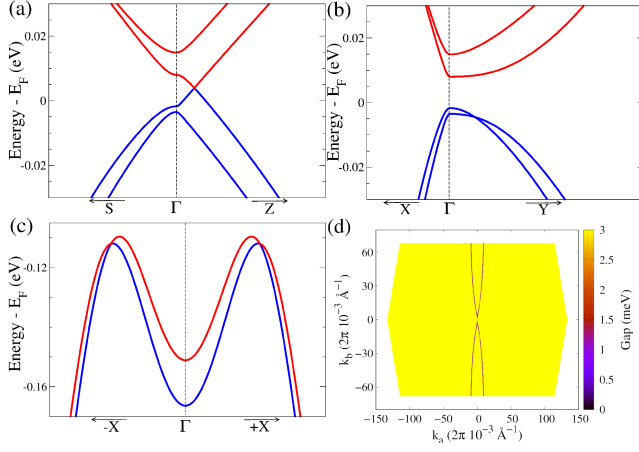


FIG. 5. (a)-(c) Band structures when \mathbf{B} field is parallel to the c axis. For (c), k_y is fixed to be $0.034100 \text{ } 2\pi \cdot \text{\AA}^{-1}$. (d) Type-II nodal ring in the k_a - k_b plane with the gap size in color scale. Here the yellow region indicates the whole first BZ.

but two gapless points, transforming into a pair of type-I Weyl nodes ($\chi_n = \pm 1$) lying in the k_a - k_b plane. As the polar angle ϕ between the \mathbf{B} field and the a axis further decreases, the Weyl points initially close to the k_a axis evolve toward the k_b axis in the k_a - k_b plane. Then when the \mathbf{B} field aligns with the a axis ($\phi = 0$), the pair of Weyl points suddenly transforms into a nodal ring in the k_b - k_c plane (with the restoration of a mirror symmetry). As the \mathbf{B} field continues to rotate clockwise beyond the positive a axis ($\phi < 0$), the nodal ring transforms into a pair of Weyl points where the chirality of the Weyl points is now exchanged. For example, Fig. 6(h) exhibits the calculated Berry curvature with a pair of Weyl nodes obtained from the WFTB model at $\phi = 45^\circ$. Figure 6(i) summarizes the calculated evolution of the nodal ring and Weyl points as a function of ϕ for $0 \leq \phi \leq 90^\circ$, where the intercepts with the k_a and k_b axes become part of the nodal rings (not drawn) when $\phi = 90^\circ$ and $\phi = 0$, respectively.

In contrast to a common belief, our result demonstrates that there is another way to annihilate Weyl points other than bringing a pair of Weyl points with opposite chirality to the same k point. This possibility was earlier discussed within effective models in the case of Dirac semimetals in the presence of \mathbf{B} field²⁴. Furthermore, our finding indicates that the chirality of the Weyl nodes can be exchanged with the reversal of the b component of the \mathbf{B} field.

E. Magnetic field in the ac or bc plane

When the \mathbf{B} field is rotated from the c axis in the bc plane, we find that the pair of type-I Weyl nodes with $\chi_n = \pm 1$ (arising from the conduction and valence bands) move somewhat away from the k_c axis and return to the

axis as the angle θ approaches 90° , where θ is the angle between the \mathbf{B} field and the c axis. See Fig. 7(a). Then when the \mathbf{B} field aligns with the b axis, the type-I Weyl points [Fig. 7(c)] abruptly transform into the type-I nodal ring in the k_a - k_c plane, as discussed earlier. For $\theta > 90^\circ$, a pair of Weyl nodes reappear with the reversed topological charges compared to those in the case of $\theta < 90^\circ$, similarly to Sec. IV D. The transformation of the Weyl nodes into a nodal ring is related to the mirror anomaly²⁴, which is discussed later in Sec. V C.

On the other hand, the type-II nodal ring arising from the top two valence bands is now completely gapped out except for two type-II gapless points [Fig. 7(d)] when the \mathbf{B} field is rotated from the c axis in the bc plane. For example, the type-II Weyl nodes occur at $(0, \pm 0.002140, \pm 0.000025) \text{ } 2\pi \cdot \text{\AA}^{-1}$ at $\theta = 10^\circ$. We confirm that the type-II gapless points have topological charge $\chi_n = \mp 1$, using the method discussed in Ref.³⁸. The type-II Weyl nodes with opposite chirality are brought closer to each other as θ increases. They are eventually annihilated when θ approaches about 40° [Fig. 7(b)].

When the \mathbf{B} field is rotated from the c axis in the ac plane, we find that the pair of type-I Weyl nodes with $\chi_n = \pm 1$ (arising from the conduction and valence bands) remain almost along the k_c axis with only slight changes in their locations. Then when the \mathbf{B} field is parallel to the a axis, the Weyl nodes transform into a nodal ring. In contrast to the case with the \mathbf{B} field in the bc plane, there are no crossings from the top two valence bands in this case.

F. Summary of topological phases from WFTB model

Table I summarizes the topological phases found from the WFTB model. In the next section, we discuss the linearized $k \cdot p$ model and the topological phases predicted from the $k \cdot p$ model. We also compare the findings from the WFTB model and those from the $k \cdot p$ model.

V. COMPARISON WITH LINEARIZED $k \cdot p$ MODEL

A. Lowest-order $k \cdot p$ model

The lowest-order $k \cdot p$ Hamiltonian $\mathcal{H}_{kp}(\mathbf{k}, \mathbf{B})$ ¹⁵ can be obtained by keeping only linear terms in \mathbf{k} that satisfy the symmetries of bulk ZrTe_5 . The Hamiltonian $\mathcal{H}_{kp}(\mathbf{k}, \mathbf{B})$ expanded near the Γ point reads

$$\mathcal{H}_{kp}(\mathbf{k}, \mathbf{B}) = \mathcal{H}_{kp,0}(\mathbf{k}) + \mathcal{H}_{kp,Z} \quad (8)$$

$$\mathcal{H}_{kp,0}(\mathbf{k}) = m\tau^z + v_x k_x \tau^x \sigma^y + v_y k_y \tau^x \sigma^x + v_z k_z \tau^y (9)$$

$$\mathcal{H}_{kp,Z} = \frac{1}{2} g \mu_B \sigma \cdot \mathbf{B}, \quad (10)$$

where $\tau^{x,y,z}$ and $\sigma^{x,y,z}$ are orbital (conduction and valence bands) and spin Pauli matrices. Here $v_{x,y,z}$ and m

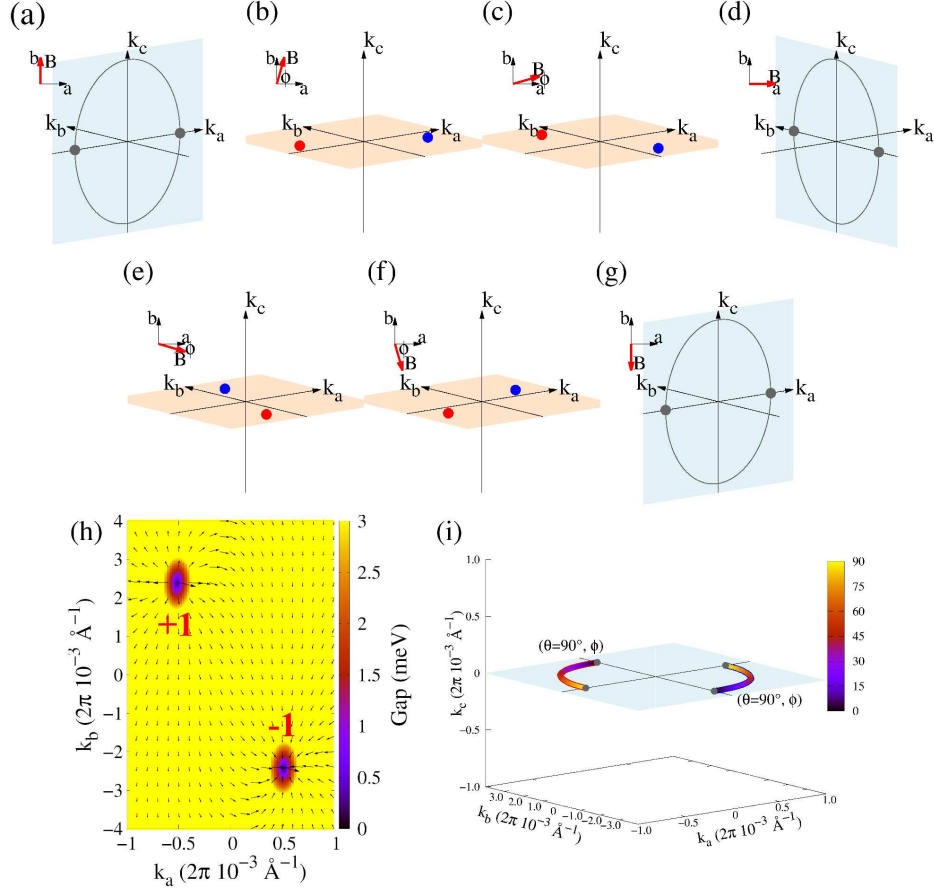


FIG. 6. (a)-(g) Schematic evolution of the nodal ring and Weyl points as a function of the angle between \mathbf{B} field and the a axis, ϕ , (h) WFTB-calculated Berry curvature in the k_a - k_b plane at $\phi = 45^\circ$, and (i) WFTB-calculated evolution of the nodal structure as a function of ϕ , when the \mathbf{B} field is in the ab plane. In (a), (d), and (g), the blue plane indicates the mirror-symmetry plane where the topological nodal ring resides. In (b), (c), (e), and (f), the red and blue filled circles correspond to Weyl points with topological charge χ of +1 and -1, respectively. In (h), the topological charge of the Weyl points is denoted, and the energy gap is shown in color scale. In (i), the color scale indicates the value of ϕ .

are Fermi velocities and mass (or half of the bulk band gap), respectively. The x , y , and z coordinates correspond to the crystal a , b , and c axes. $\mathcal{H}_{\text{kp,Z}}$ is the Zeeman interaction where we assume the same isotropic g -factors for the conduction and valence bands for simplicity. The

symmetry group of ZrTe_5 is generated by two mirror reflections, M_{ab} , M_{bc} , inversion and time-reversal symmetries, which are represented by $-\tau^z \cdot i\sigma^z$, $i\sigma^x$, τ^z , and $\mathcal{K} \cdot i\sigma^y$, respectively (\mathcal{K} is complex conjugation).

Equation (8) can be diagonalized for an arbitrary \mathbf{B} field with energy eigenvalues given by

$$\epsilon_{rs}(\mathbf{k}, \mathbf{B}) = r \sqrt{m^2 + \left(\frac{g\mu_B}{2} \right)^2 B_0^2 + K^2 + s \sqrt{m^2 B_0^2 + (v_z k_z)^2 B_0^2 + A_\perp^2 g\mu_B}}, \quad (11)$$

where $r, s = \pm$, $B_0^2 = B_x^2 + B_y^2 + B_z^2$, $K^2 = (v_x k_x)^2 + (v_y k_y)^2 + (v_z k_z)^2$, and $A_\perp^2 = (v_x k_x B_y + v_y k_y B_x)^2$. In Ref.¹⁵ only three \mathbf{B} field directions (a , b , and c axes) are considered. The energy eigenvalues, Eq. (11), agree with those in Ref.¹⁵. We find that the conduction and valence

bands can cross if the Zeeman splitting energy is greater than the band gap, i.e., $(\frac{g\mu_B B_0}{2})^2 > m^2$, whereas the two conduction (valence) bands can not cross each other for any \mathbf{B} field directions. The resulting nodal structure is summarized in Table I.

TABLE I. Zeeman-splitting driven topological phases in 3D ZrTe₅ as a function of the \mathbf{B} -field orientation based on the WFTB model and the linearized $k \cdot p$ model¹⁵ (discussed in Sec. V), considering the energy window of $[-0.12, 0.05]$ eV relative to the Fermi level. The second column corresponds to the nodal structure from the crossings of the bottom conduction and the top valence bands, and the third column for that of the top two valence bands in the WFTB model. In the case of the $k \cdot p$ model, the top two valence bands never meet. The topological phase for the \mathbf{B} field within the ab , bc , or ac plane (marked by *) excludes the cases that the \mathbf{B} field coincides with the a , b , or c axis. In the case of WFTB (VB-VB), the type-II Weyl nodes (marked by \dagger) are formed for only some angles ($< 40^\circ$) before they meet and annihilate at the same k point, as in Fig. 7(b).

Direction \ Model	WFTB (CB-VB)	WFTB (VB-VB)	$k \cdot p$ (CB-VB)
$\mathbf{B} \parallel \mathbf{a}$	1 type-I nodal ring	-	1 type-I nodal ring
$\mathbf{B} \parallel \mathbf{b}$	1 type-I nodal ring	-	1 type-I nodal ring
$\mathbf{B} \parallel \mathbf{c}$	2 type-I Weyl nodes	1 type-II nodal ring	2 type-I Weyl nodes
\mathbf{B} in ab plane*	2 type-I Weyl nodes	-	1 type-I nodal ring
\mathbf{B} in bc plane*	2 type-I Weyl nodes	2 type-II Weyl nodes †	2 type-I Weyl nodes
\mathbf{B} in ac plane*	2 type-I Weyl nodes	-	2 type-I Weyl nodes

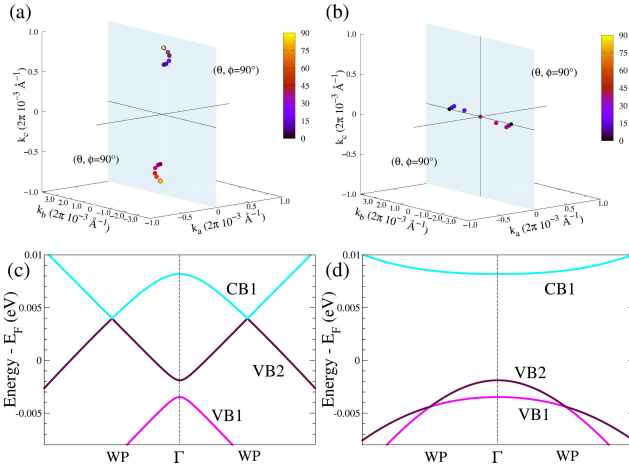


FIG. 7. (a)-(b) WFTB-calculated evolution of the type-I and type-II Weyl nodes, respectively, as a function of θ (color scale) when the \mathbf{B} field rotates in the bc plane. The type-I Weyl nodes arise from the crossings of the conduction and valence bands, whereas the type-II Weyl nodes arise from the two valence bands. Here ϕ is the angle between \mathbf{B} field and the a axis. In (a) the Weyl points are located at $(0, \pm 0.000540, \mp 0.000757) 2\pi \cdot \text{\AA}^{-1}$ for $\theta = 45^\circ$. (c)-(d) WFTB-calculated band structures near the crossings of the conduction (CB1) and valence bands (VB2) and of the two valence bands (VB1 and VB2) for the \mathbf{B} field in the bc plane with $\theta=10^\circ$.

B. Comparison between WFTB and lowest-order $k \cdot p$ models

The nodal structure calculated using the WFTB and lowest-order $k \cdot p$ models qualitatively agree with each other in most cases, as listed in Table I, although the positions of Weyl points or nodal rings may quantitatively differ from each other. The previous study¹⁵ reported the nodal structure only when the \mathbf{B} field aligns with the crystal axes using the lowest-order $k \cdot p$ model. *Qualitative* discrepancy between the WFTB model and the

lowest-order $k \cdot p$ model occurs in two cases: (i) when the top two valence bands meet with each other for the \mathbf{B} field along the c axis and in the bc plane and (ii) when the \mathbf{B} field lies in the ab plane (though not along the a or b axes). The first discrepancy might arise from the observation that Zr d orbitals contribute to the top two valence bands by about 20% of the total electron density according to our DFT calculations, whereas the lowest-order $k \cdot p$ model¹⁵ was constructed based on Te p orbitals only. The second discrepancy arises from the extra symmetry imposed on the lowest $k \cdot p$ model due to truncation of higher-order terms.

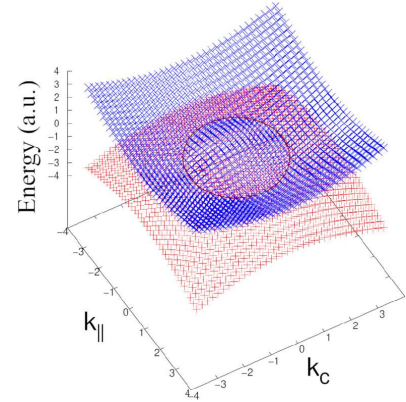


FIG. 8. Calculated gapless nodal points in the k_{\parallel} - k_c plane when the \mathbf{B} field is tilted by 45° from the a axis in the ab plane, using the lowest-order $k \cdot p$ model, where k_{\parallel} is the direction along the $k_a = k_b$ line. The nodal ring is marked in red. All parameter values are set to unity for simplicity.

When the \mathbf{B} field aligns with either the a or b axis, a nodal ring appears in the corresponding mirror plane. Interestingly, in the lowest-order $k \cdot p$ model, we find that this nodal ring persists as long as the \mathbf{B} field lies in the ab plane, even though there is *no* mirror symmetry that protects the nodal ring when the \mathbf{B} field is away from the a or b axis. For example, Fig. 8 shows the calculated nodal ring using the lowest $k \cdot p$ model when the angle

between the \mathbf{B} field and the a axis is 45° . Compare this figure to the nodal structure obtained from the WFTB model [Fig. 6(h)] for the same \mathbf{B} field direction. Our study shows that continuous $U(1)$ symmetry is present in the lowest-order $k \cdot p$ model, which rotates both the band structure and the \mathbf{B} field together about the c axis. This symmetry is represented by

$$U(\theta)\mathcal{H}_{\text{kp}}(\mathbf{k}, \mathbf{B})U^\dagger(\theta) = \mathcal{H}_{\text{kp}}(R(\theta)\mathbf{k}, R^{-1}(\theta)\mathbf{B}) \quad (12)$$

where

$$U(\theta) = \begin{bmatrix} e^{-i\theta/2} & 0 & 0 & 0 \\ 0 & e^{i\theta/2} & 0 & 0 \\ 0 & 0 & e^{-i\theta/2} & 0 \\ 0 & 0 & 0 & e^{i\theta/2} \end{bmatrix}, \quad (13)$$

and

$$R(\theta) = \begin{bmatrix} \cos \theta & \sin \theta & 0 \\ -\sin \theta & \cos \theta & 0 \\ 0 & 0 & 1 \end{bmatrix}. \quad (14)$$

For simplicity, we assume an isotropic Fermi velocity and an isotropic g -factor, but a similar result holds in general cases. However, higher-order terms in the $k \cdot p$ model would break the $U(1)$ symmetry, and they would gap out the nodal ring unless there is mirror symmetry. Neither the WFTB model nor the crystal structure of ZrTe_5 have such $U(1)$ symmetry.

C. Mirror anomaly

Recently, Burkov²⁴ has pointed out an additional quantum anomaly referred to as mirror anomaly inherent in Dirac semimetals with mirror symmetry, independent of their type or origin such as topological⁷, nonsymmorphic¹⁰, or accidental, based on the linearized Dirac Hamiltonian. In a Dirac semimetal, the chirality operator $\gamma^5 = i\gamma^0\gamma^1\gamma^2\gamma^3$ (which projects chirality of the two Weyl fermion components)^{23,24} commutes with only one of the spin components. When the \mathbf{B} field rotates from this spin direction to the perpendicular axis with which mirror symmetry is present, the Weyl points abruptly transform into a nodal ring protected by the mirror symmetry. Furthermore, in the Dirac Hamiltonian, the positions of the Weyl nodes do not change with rotation angle until they become the nodal ring. As a consequence, intrinsic AHC was predicted to show a singular behavior as a function of the \mathbf{B} field direction.

In the lowest-order $k \cdot p$ model for ZrTe_5 , Eq. (8), the spin component that commutes with the chirality operator is the c or z component. Therefore, in the $k \cdot p$ model, the mirror anomaly dictates the abrupt transformation of a pair of Weyl points into a nodal ring as well as singular intrinsic out-of-plane AHC when the \mathbf{B} field rotates from the c axis to the a or b axis. The difference between the

WFTB model and the $k \cdot p$ model in this context is that the positions of the Weyl points noticeably change with the \mathbf{B} -field orientation when the field is in the bc plane in the WFTB model.

VI. INTRINSIC ANOMALOUS HALL EFFECT

When Weyl points are present at the Fermi level, the material can manifest large AHC despite the point-like Fermi surface, which serves as an important experimental signature for Weyl semimetals. In general, broken time reversal symmetry along with a finite-volume Fermi surface may give rise to nonzero AHC whether Weyl points are present or not.

A. Numerical calculation of AHC

We numerically compute the AHC σ_{ac} of ZrTe_5 under an external \mathbf{B} field based on our WFTB model, as a function of chemical potential as well as the direction of \mathbf{B} field. In the next two subsections, we separately present our results in the cases of isotropic and anisotropic g factor. We consider σ_{ac} because the ac plane is perpendicular to the stacking direction, which is experimentally the most relevant plane^{15,17}. We focus on the *intrinsic* part of the AHC^{20,21} which depends only on the Berry curvature:

$$\sigma_{ac} = \frac{e^2}{h} \sum_{n=1}^{\text{occ}} \int_{\text{BZ}} \frac{d^3k}{(2\pi)^3} f(\mathcal{E}_n(\mathbf{k}) - \mu) \Omega_{n,b}(\mathbf{k}), \quad (15)$$

$$= \frac{e^2}{h} \int_{k_b} \frac{dk_b}{2\pi} C(k_b), \quad (16)$$

where $f(\mathcal{E}_n(\mathbf{k}) - \mu)$ is the Fermi-Dirac distribution with chemical potential μ , and $\Omega_{n,b}(\mathbf{k})$ is the b -component of the Berry curvature coming from the n -th band. Here $C(k_b)$ is the Chern number (considering all occupied bands) calculated at a given k_b plane. We assume that temperature is zero. Regarding the 3D integral of the whole first BZ in Eq. (15), we perform 2D integrals in the k_a - k_c plane ($\sigma_{ac,k_b}^{2D} = C(k_b) \frac{e^2}{h}$) at fixed k_b planes and integrate the 2D integrals along the k_b direction. In this calculation we separate the first BZ into two regions such as near the Γ point and away from the Γ point, and use a finer (coarser) k -mesh for the former (latter) region.

When the Fermi surface is composed of a pair of isolated Weyl points with topological charge $\pm\chi$, $|\sigma_{ac}|$ is known to be $\frac{e^2}{h} \frac{2k_b^{\text{WP}}}{2\pi} |\chi|$, where $2k_b^{\text{WP}}$ is the separation between the two Weyl points projected onto the b axis. This is because each 2D plane parallel to the ac plane which lies between the two Weyl points contributes Chern number of χ or $-\chi$ to the integral in Eq. (16), whereas the planes which do not lie between the two Weyl points have zero Chern number. In this case, the intrinsic AHC is simply proportional to the separation between the Weyl

points along the b axis. However, if the Fermi surface has a nonzero volume, there is no such a simple expression for σ_{ac} and the AHC must be numerically computed.

Equation (15) enforces that σ_{ac} is strictly zero if the \mathbf{B} field is parallel to the ac plane due to the $C_{2b}\mathcal{T}$ symmetry. The $C_{2b}\mathcal{T}$ symmetry maps the Berry curvature component $\Omega_b(k_a, k_b, k_c)$ into $-\Omega_b(k_a, -k_b, k_c)$, making the integral in Eq. (15) vanish. Therefore, the nonzero AHC observed in Ref.¹⁷ for the in-plane \mathbf{B} fields (i.e. parallel to the ac plane) must originate from the non-intrinsic part of the AHC and/or nonlinear effects.

B. Calculated AHC in the case of isotropic g factor

Figure 9(a) shows numerically calculated σ_{ac} as a function of chemical potential when the \mathbf{B} field rotates in the ab plane, in the case of isotropic g factor. First of all, we find that intrinsic σ_{ac} becomes strictly zero independent of the chemical potential value when the \mathbf{B} field exactly aligns with the a axis due to the symmetry argument provided earlier. Let us first discuss features at chemical potential $\mu = -4$ meV (referred to as μ_2) which coincides with the type-I Weyl point energy. See Fig. 10(a). At this chemical potential, a sharp, prominent (negative) peak appears for all angles except for 0° and 90° . The peak height varies with ϕ , as shown in Fig. 9(d). In order to provide more insight, we also calculate σ_{ac,k_b}^{2D} at different k_b planes, finding that they are quantized as either 0 or -1 in units of $\frac{e^2}{h}$. This result explains both the peak height $\sim \frac{e^2}{h} \frac{2k_b^{WP}}{2\pi}$ and the angular evolution of the peak height. The abrupt increase in the peak height is attributed to the large separation of the Weyl point along the b axis as the angle increases from zero. The peak height, however, goes to zero smoothly as the angle approaches 90° because of the smooth changes of the Weyl point separation. See Fig. 6(i). In addition to the sharp peak, smoothly rising negative and positive peaks appear near $+6$ meV (μ_1) and $+14$ meV (μ_3) for large angles ($\geq 60^\circ$). See Figs. 9(a), (c), and (e). Note that there are no other Weyl nodes beyond the pair discussed earlier. Now the σ_{ac,k_b}^{2D} values for μ_1 and μ_3 are not quantized in units of $\frac{e^2}{h}$ [Fig. 10(b)]. However, they contribute to the σ_{ac} value, Eq. (15), via avoided level crossings as shown in Fig. 10(a). Our result is not unusual. For example, in bcc Fe, Co, and Ni, a very large Berry curvature was found in regions where avoided level crossings occur, and it resulted in large AHC³⁷.

Now when the \mathbf{B} field rotates from the c axis in the bc plane, overall features of σ_{ac} [Figs. 9(b), (f)-(h)] are similar to those for the above case, though with some differences. Let us first discuss σ_{ac} at chemical potential μ_2 . At this chemical potential, the height of the negative peak can be up to an order of magnitude smaller than that for the above case, as shown in the inset of Fig. 9(b) and Fig. 9(g). The σ_{ac,k_b}^{2D} values are quantized as either 0 or -1 in units of $\frac{e^2}{h}$. For example, Fig. 10(c) and (d) show

such quantization for $\theta = 10$ and 40° . The observed peak height of $\frac{e^2}{h} \frac{2k_b^{WP}}{2\pi}$ also corroborates the contributions of the type-I Weyl points which evolve with the angle as illustrated in Fig. 7(a). Next, for $0 < \mu < 8$ meV, the flat σ_{ac} region arises from contributions of small nonzero σ_{ac,k_b}^{2D} values near Γ . See upward-triangles in Fig. 10(c) and (d). Last, at $\mu = -3.5$ meV a small positive peak appears only for small angles ($< 40^\circ$). This peak is associated with the type-II Weyl nodes arising from the crossings of the two valence bands. See Fig. 7(d). At higher angles, the type-II Weyl points with opposite chirality are annihilated, and the σ_{ac} peak vanishes accordingly.

C. Calculated AHC in the case of anisotropic g factor

Figure 11(a) shows our calculated σ_{ac} as a function of μ and ϕ , using the following anisotropic g factors: $g_x=3.19^{33}$, $g_y=21.3^{15,33}$, and $g_z=2.0$. In this case, the Zeeman energy remains to be fixed as 10 meV. In other words, $\sqrt{g_x^2 B_x^2 + g_y^2 B_y^2 + g_z^2 B_z^2} = 10$ meV. When the \mathbf{B} field rotates from the a axis in the ab plane, the height of the sharp AHC peak at μ_2 abruptly increases with the angle and then it immediately starts to decrease. See Fig. 11(d). On the other hand, the height of the smooth peaks at μ_1 and μ_3 sharply increases with the angle and then it saturates at a small angle. See Fig. 11(c) and (e). These features can be explained using the Weyl-point positions and avoided level crossings, similarly to the case of isotropic g factor.

A similar trend appears when the \mathbf{B} field is tilted in the bc plane [Figs. 11(b), (f)-(h)]. One small difference is shown in the inset of Fig. 11(b). The small AHC peak at μ_2 vanishes for very large angles such as $80 \leq \theta < 90^\circ$, because the b component of the Weyl point position becomes zero.

Overall the angular dependence of σ_{ac} with the anisotropic g factor qualitatively differs from that with the isotropic g factor in both ab and bc planes. This is attributed to a much larger contribution of the b component of \mathbf{B} field for a given angle. For the same reason, with the anisotropic g factor, the type-II Weyl nodes are not formed except for extremely small angles away from the c axis. Note that the type-II Weyl nodes with opposite chirality are annihilated at $\theta \geq 40^\circ$ in the case of isotropic g factor.

VII. CONCLUSION

In summary, we develop a WFTB model for 3D ZrTe₅ from first-principles calculations, considering both Zr d and Te p orbitals. Based on the WFTB model, we investigate Zeeman-splitting induced topological phases and the evolution of the topological nodal structures as a function of the orientation of \mathbf{B} field (beyond the crystal

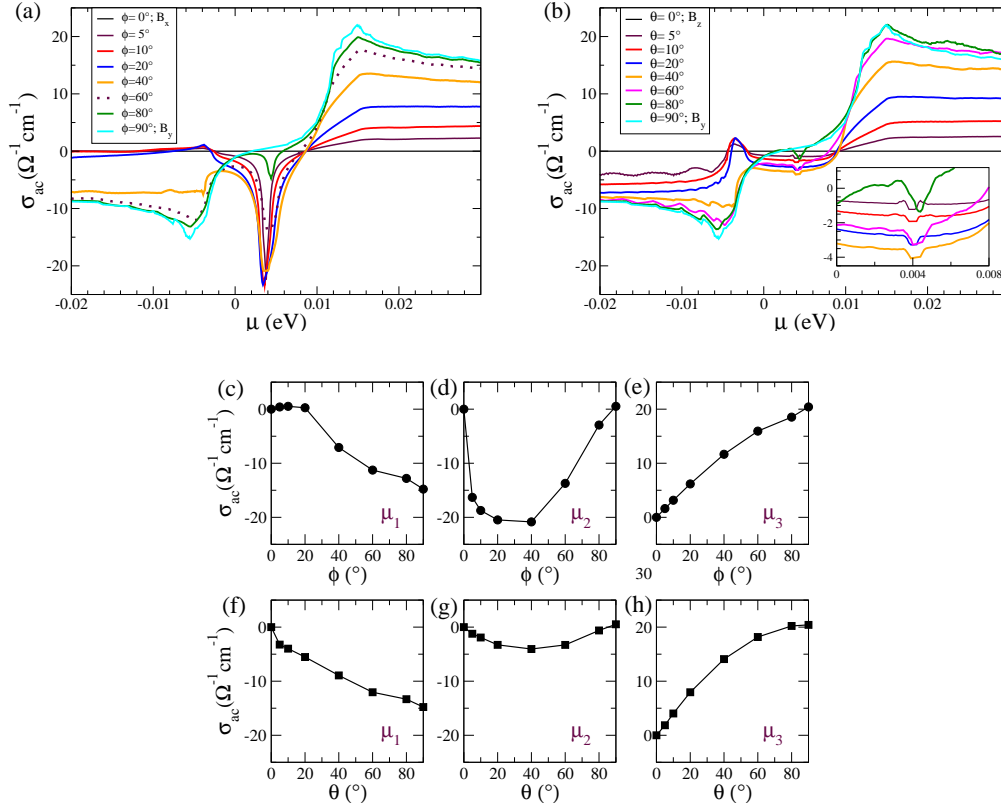


FIG. 9. WFTB-calculated AHC σ_{ac} as a function of chemical potential μ and tilting angles ϕ and θ when the \mathbf{B} field is parallel to (a) the ab plane or (b) the bc plane, in the case of isotropic g factor. Here ϕ is the angle between the \mathbf{B} field and the a axis, and θ is the angle between the \mathbf{B} field and the c axis. The Fermi level is set to $\mu = 0$. (c)-(h) Calculated σ_{ac} vs ϕ and θ at three chemical potential values, μ_1 (-6 meV), μ_2 (4 meV), and μ_3 (14 meV). The μ_2 value is close to the type-I Weyl point energy. The inset in (b) shows zoom-in near the μ_2 value.

axes). We find an abrupt transformation of a nodal ring to a pair of Weyl nodes as the \mathbf{B} field is rotated from either the crystal a or b axis. At some \mathbf{B} field directions type-II nodal structures are identified from crossings of the valence bands. Comparing the calculated topological phases with those from the linearized $k \cdot p$ model, we find that the latter model does *not* capture the correct topological phases when the \mathbf{B} field is rotated in the ab or in bc plane. We also numerically compute the intrinsic part of the AHC, σ_{ac} , as a function of chemical potential, when the \mathbf{B} field is tilted within the ab or bc plane. The calculated results can be compared to the experimental data when the experimental anomalous Hall resistivity ρ_{ac}^{AHE}

is properly converted into σ_{ac} , which requires the knowledge of longitudinal resistivity. Our findings may also provide insight into Zeeman-splitting-induced topological phases and their consequences in other Dirac semimetals with mirror symmetries.

ACKNOWLEDGMENTS

Y.C. was supported by the Virginia Tech ICTAS Fellowship. The computational support was provided by San Diego Supercomputer Center (SDSC) under DMR060009N and VT Advanced Research Computing (ARC).

* yichul00@vt.edu

† jvillano@uark.edu

‡ kyungwha@vt.edu

¹ H. Weng, X. Dai, and Z. Fang, Phys. Rev. X **4**, 011002 (2014).

² Z. Fan, Q.-F. Liang, Y. B. Chen, S.-H. Yao, and J. Zhou, Sci. Rep. **7**, 45667 (2017).

³ J. Mutch, W.-C. Chen, P. Went, T. Qian, I. Z. Wilson, A. Andreev, C.-C. Chen, and J.-H. Chu, Sci. Adv. **5**, eaav9771 (2019).

⁴ Y. Zhang, C. Wang, L. Yu, G. Liu, A. Liang, J. Huang, S. Nie, X. Sun, Y. Zhang, B. Shen, J. Liu, H. Weng, L. Zhao, G. Chen, X. Jia, C. Hu, Y. Ding, W. Zhao, Q. Gao, C. Li, S. He, L. Zhao, F. Zhang, S. Zhang, F. Yang,

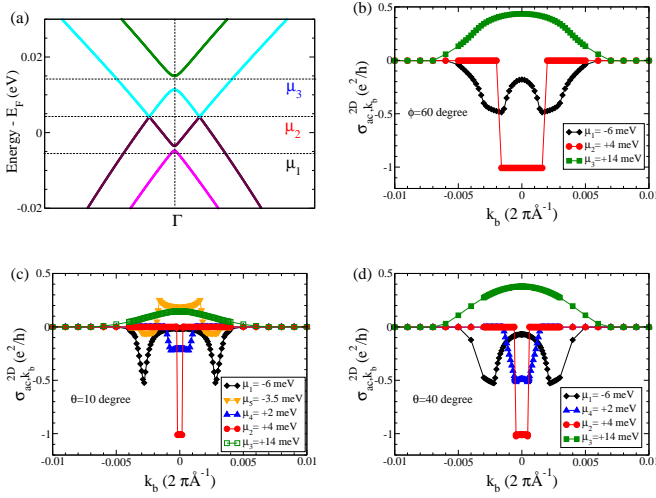


FIG. 10. (a) WFTB-calculated band structure along the Weyl-point separation direction and (b) σ_{ac,k_b}^{2D} at fixed k_b values vs k_b for three different chemical potential values, when the \mathbf{B} field is tilted from the a axis by 60° in the ab plane. (c)-(d) Calculated σ_{ac,k_b}^{2D} vs k_b for different chemical potential values, when the \mathbf{B} field is tilted from the c axis by 10° or 40° in the bc plane, respectively. Here $\mu_5 = -3.5$ meV corresponds to the energy of the small positive AHC peak right below the Fermi level for $\theta=5, 10$, and 20° . The type-II Weyl-point energy is -4.5 meV. In (a)-(d) we consider the isotropic g factor.

Z. Wang, Q. Peng, X. Dai, Z. Fang, Z. Xu, C. Chen, and X. J. Zhou, Nat. Commun. **8**, 15512 (2017).

⁵ B. Xu, L. X. Zhao, P. Marsik, E. Sheveleva, F. Lyzwa, Y. M. Dai, G. F. Chen, X. G. Qiu, and C. Bernhard, Phys. Rev. Lett. **121**, 187401 (2018).

⁶ R. Noguchi, T. Takahashi, K. Kuroda, M. Ochi, T. Shirasawa, M. Sakano, C. Bareille, M. Nakayama, M. D. Watson, K. Yaji, A. Harasawa, H. Iwasawa, P. Dudin, T. K. Kim, M. Hoesch, V. Kandyba, A. Giampietri, A. Barinov, S. Shin, R. Arita, T. Sasagawa, and T. Kondo, Nature **566**, 518 (2019).

⁷ B.-J. Yang and N. Nagaosa, Nat. Commun. **5**, 4898 (2014).

⁸ Z. Wang, Y. Sun, X.-Q. Chen, C. Franchini, G. Xu, H. Weng, X. Dai, and Z. Fang, Phys. Rev. B **85**, 195320 (2012).

⁹ Z. Wang, H. Weng, Q. Wu, X. Dai, and Z. Fang, Phys. Rev. B **88**, 125427 (2013).

¹⁰ S. M. Young, S. Zaheer, J. C. Y. Teo, C. L. Kane, E. J. Mele, and A. M. Rappe, Phys. Rev. Lett. **108**, 140405 (2012).

¹¹ H. Xiong, J. A. Sobota, S.-L. Yang, H. Soifer, A. Gauthier, M.-H. Lu, Y.-Y. Lv, S.-H. Yao, D. Lu, M. Hashimoto, P. S. Kirchmann, Y.-F. Chen, and Z.-X. Shen, Phys. Rev. B **95**, 195119 (2017).

¹² Y.-Y. Lv, B.-B. Zhang, X. Li, K.-W. Zhang, X.-B. Li, S.-H. Yao, Y. B. Chen, J. Zhou, S.-T. Zhang, M.-H. Lu, S.-C. Li, and Y.-F. Chen, Phys. Rev. B **97**, 115137 (2018).

¹³ G. Manzoni, L. Gragnaniello, G. Autès, T. Kuhn, A. Sterzi, F. Cilento, M. Zacchigna, V. Enenkel, I. Vobornik, L. Barba, F. Bisti, P. Bugnon, A. Magrez, V. N. Strocov, H. Berger, O. V. Yazyev, M. Fonin, F. Parmigiani, and A. Crepaldi, Phys. Rev. Lett. **117**, 237601 (2016).

¹⁴ J. L. Zhang, C. Y. Guo, X. D. Zhu, L. Ma, G. L. Zheng, Y. Q. Wang, L. Pi, Y. Chen, H. Q. Yuan, and M. L. Tian, Phys. Rev. Lett. **118**, 206601 (2017).

¹⁵ R. Y. Chen, Z. G. Chen, X.-Y. Song, J. A. Schneeloch, G. D. Gu, F. Wang, and N. L. Wang, Phys. Rev. Lett. **115**, 176404 (2015).

¹⁶ J. Wang, J. Niu, B. Yan, X. Li, R. Bi, Y. Yao, D. Yu, and X. Wu, Proc. Natl. Acad. Sci. USA **115**, 9145 (2018).

¹⁷ T. Liang, J. Lin, Q. Gibson, S. Kushwaha, M. Liu, W. Wang, H. Xiong, J. A. Sobota, M. Hashimoto, P. S. Kirchmann, Z.-X. Shen, R. J. Cava, and N. P. Ong, Nat. Phys. **14**, 451 (2018).

¹⁸ J. Ge, D. Ma, Y. Liu, H. Wang, Y. Li, J. Luo, T. Luo, Y. Xing, J. Yan, D. Mandrus, H. Liu, X. C. Xie, and J. Wang, (2019), arXiv:1905.06040.

¹⁹ F. Tang, Y. Ren, P. Wang, R. Zhong, J. Schneeloch, S. A. Yang, K. Yang, P. A. Lee, G. Gu, Z. Qiao, and L. Zhang, Nature **569**, 537 (2019).

²⁰ D. Xiao, M.-C. Chang, and Q. Niu, Rev. Mod. Phys. **82**, 1959 (2010).

²¹ N. Nagaosa, J. Sinova, S. Onoda, A. H. MacDonald, and N. P. Ong, Rev. Mod. Phys. **82**, 1539 (2010).

²² S. Nandy, G. Sharma, A. Taraphder, and S. Tewari, Phys. Rev. Lett. **119**, 176804 (2017).

²³ A. A. Burkov, Phys. Rev. B **96**, 041110 (2017).

²⁴ A. A. Burkov, Phys. Rev. Lett. **120**, 016603 (2018).

²⁵ H. Fjellvåg and A. Kjekshus, Solid State Commun. **60**, 91 (1986).

²⁶ G. Kresse and J. Furthmüller, Phys. Rev. B **54**, 11169 (1996).

²⁷ G. Kresse and J. Furthmüller, Comput. Mater. Sci. **6**, 15 (1996).

²⁸ A. A. Mostofi, J. R. Yates, G. Pizzi, Y.-S. Lee, I. Souza, D. Vanderbilt, and N. Marzari, Comput. Phys. Commun. **185**, 2309 (2014).

²⁹ J. P. Perdew, K. Burke, and M. Ernzerhof, Phys. Rev. Lett. **77**, 3865 (1996).

³⁰ P. E. Blöchl, Phys. Rev. B **50**, 17953 (1994).

³¹ N. Marzari and D. Vanderbilt, Phys. Rev. B **56**, 12847 (1997).

³² I. Souza, N. Marzari, and D. Vanderbilt, Phys. Rev. B **65**, 035109 (2001).

³³ Y. Liu, X. Yuan, C. Zhang, Z. Jin, A. Narayan, C. Luo, Z. Chen, L. Yang, J. Zou, X. Wu, S. Sanvito, Z. Xia, L. Li, Z. Wang, and F. Xiu, Nat. Commun. **7**, 12516 (2016).

³⁴ L. Fu and C. L. Kane, Phys. Rev. B **76**, 045302 (2007).

³⁵ Q. Wu, S. Zhang, H.-F. Song, M. Troyer, and A. A. Soluyanov, Comput. Phys. Commun. **224**, 405 (2018).

³⁶ J. W. Villanova and K. Park, Phys. Rev. B **98**, 075123 (2018).

³⁷ X. Wang, D. Vanderbilt, J. R. Yates, and I. Souza, Phys. Rev. B **76**, 195109 (2007).

³⁸ A. A. Soluyanov, D. Gresch, Z. Wang, Q. Wu, M. Troyer, X. Dai, and B. A. Bernevig, Nature **527**, 495 (2015).

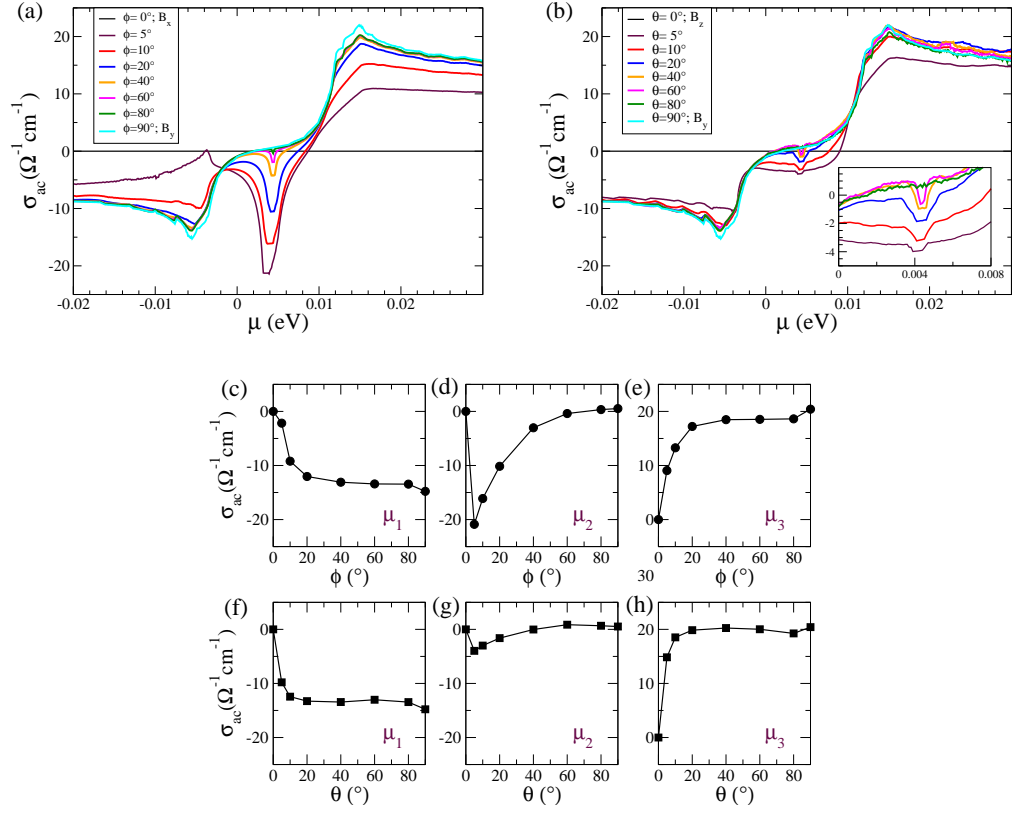


FIG. 11. WFTB-calculated AHC σ_{ac} as a function of μ , ϕ and θ when the \mathbf{B} field is parallel to the ab plane (a) or the bc plane (b), in the case of *anisotropic* g factor. (c)-(h) Calculated σ_{ac} vs ϕ and θ at μ_1 (-6 meV), μ_2 (4 meV), and μ_3 (14 meV). The μ_2 value is close to the type-I Weyl point energy. The inset in (b) shows zoom-in near the μ_2 value.